Breaking onset and breaking strength of focused wave packets: Linear prediction model and nonlinear numerical simulations

Hulin Florian [1, 2, 3, *], Prevosto Marc [1, 4], Tassin Alan [2], Filipot Jean-François [1], Jacques Nicolas [3], Grilli Stephan [5]

[1] France Énergies Marines, Plouzané, France
[2] Ifremer, RDT, F-29280 Plouzané, France
[3] ENSTA Bretagne, UMR CNRS 6027, IRDL, 29806 Brest Cedex 09, France
[4] Independent researcher, 29200 Brest, France
[5] Department of Ocean Engineering, University of Rhode Island, Narragansett, RI 02882, USA

* Corresponding author : Florian Hulin, email address : florian.hulin@ec-nantes.fr

Abstract :

The possibility of predicting the occurrence of wave breaking and the intensity of the breaking events using linear wave models is investigated. For this purpose, a new linear breaking onset criterion is proposed, based on the definition of a linear-equivalent wave, which has the same energy and impulse as the associated nonlinear wave. The strength of breaking is characterized by the parameter introduced by Derakhtiet al. (2018) and we derive an empirical law to estimate the breaking strength from the linear-equivalent wave model. The predictive ability of this criterion is assessed through comparisons with results of fully nonlinear potential flow simulations, for focused wave packets of various characteristics. For the considered configurations, the proposed approach is able to predict the onset and strength of breaking with good accuracy.

Highlights

► Linear wave theory can be used to estimate breaking of focused waves. ► Linear wave theory allows to predict the breaking strength of focused waves. ► Important time and spatial shifts observed when generating focused breaking waves are due to linear effects. ► The breaking strength of a wave depends on the local steepness at breaking and not on the global steepness of the wave packet.

Keywords : Breaking waves, Breaking probabilities, Fully nonlinear potential flow modeling

1. Introduction

Wave breaking is a complex phenomenon which, for a long time, has attracted the attention of scientists from many disciplines, due to its importance in different physical processes, from gas exchanges at the air-sea interface (e.g., Deike and Melville, 2018) to the critical hydrodynamic loads that breaking waves may induce on coastal and marine structures (e.g., Paulsen et al., 2019). Despite significant research efforts and progress made in the last decades (see Banner and Peregrine, 1993; Perlin et al., 2013; Deike, 2022), some aspects of this phenomenon still remain rather poorly understood. Predicting the breaking onset of a wave, i.e. whether or not the wave will evolve towards breaking, is difficult yet very important for different applications in ocean science and engineering. One common goal of many past research investigations was to identify a universal and consistent breaking onset criterion, applicable to any wave conditions, e.g., in terms of water depth, frequency content, mechanism leading to breaking, breaking strength, bathymetry... In this context, the various breaking onset criteria that have been proposed may be classified into three main categories: (i) geometric, (ii) dynamic, and (iii) kinematic criteria. To date, the likely most promising breaking onset criterion was proposed by Barthelemy et al. (2018) based on energy arguments (dynamic criterion). However, the authors showed that it reduces to a kinematic condition at the crest of the wave. The criterion states that waves will inevitably break when the fluid particle horizontal velocity at the crest, u, exceeds 85% of the crest celerity, c. This criterion, also referred to as the $B = u/c$ criterion, was validated for a wide range of breaking conditions and mechanisms such as frequency focusing (Barthelemy et al., 2018; Derakhti et al., 2018), modulational instability (Derakhti et al., 2020; Saket et al., 2017) and shoaling over a bar or a beach (Derakhti et al., 2020; Varing et al., 2021; Mohanlal et al., 2023). On the basis of numerical simulations with a Navier-Stokes model aimed at validating the B criterion, Derakhti et al. (2018) further showed that the breaking-induced energy dissipation rate b (e.g., Duncan,

1981) could be expressed as a function of a non-dimensional breaking strength parameter, Γ, defined as the non-dimensionalized time derivative of B at breaking onset:

$$\Gamma = T_b \frac{dB}{dt}\bigg|_{B=0.85}, \tag{1}$$

where T_b is a characteristic breaking wave period. Moreover, the authors observed that Γ could be related to the breaking type, with small values of Γ corresponding to spilling breakers and large values of Γ corresponding to plunging breakers. This property was later confirmed in shallow water by Mohanlal et al. (2023) based on Fully Nonlinear Potential Flow (FNPF) simulations. Quantifying the B and Γ parameters in specific situations requires accurately simulating the flow field, particularly in the wave crest region. This can be done, for instance, based on FNPF solvers, which have long been shown to predict accurately wave geometry and kinematics up to and into the early stages of the breaking process (e.g., Grilli et al., 1994, 1997; Guyenne and Grilli, 2006; Barthelemy et al., 2018) or multiphase Navier-Stokes solvers (e.g., Derakhti et al., 2018). In all the earlier studies, it was noted that both u and c needed to be carefully and accurately computed to prevent oscillating values of the B parameter. This is particularly critical for computing Γ, which involves the time-derivative of B.

Recently, under the auspice of the DIMPACT project, which was led by France Énergies Marines and was dedicated to the design of floating offshore wind turbines with respect to the water impacts induced by breaking waves, experimental and numerical investigations showed a clear correlation between wave slamming forces on a vertical cylinder and the Γ parameter of the undisturbed incoming waves (Batlle Martin et al., 2023; Hulin, 2024). These results suggest that Γ could be used to predict such forces and, hence, help in the design of marine structures exposed to breaking wave impact loads. However, the computational time and resources necessary to simulate a breaking wave event with high-fidelity numerical approaches precludes their use in practical engineering applications. For instance, the design of offshore wind turbines relies on simulating multiple 3-hour extreme sea states in order to evaluate the Ultimate Limit State (ULS). In this context, linear or weakly nonlinear approaches are most often used for such simulations. Moreover, probabilistic methodologies for the design of marine structures need statistics on the wave characteristics which are easily obtained when considering linear irregular waves, that is to say Gaussian waves. For these reasons, having a methodology based on linear wave theory that could predict the occurrence of extreme breaking wave events, their strength and the characteristics of the breaking waves (e.g., crest height, crest celerity,...) would be desirable. These parameters could, indeed, be used as inputs for breaking wave impact load models. Developing and validating such a method is the overall goal of this work. For this purpose, the breaking onset criterion, B, and the breaking strength, Γ, need to be estimated from linear wave theory. This research follows previous efforts by Stringari et al. (2021) who attempted to predict the probability of breaking based on the frequency wave energy spectrum of the sea state of interest. To do so, they derived a linear-equivalent breaking onset criterion by comparing the ratio u/c of a regular fully nonlinear deep-water wave to that of a regular linear wave of similar mechanical energy, in the same spirit as Filipot et al. (2010). They found that the ratio u/c of a linear regular wave with the same energy as that of a nearly breaking fully nonlinear wave was equal to $u/c = 0.3817$. This result is consistent with the findings of Ardag and Resio (2020), who reported that $u/c \simeq 0.4$ was relevant to distinguish breaking from non-breaking waves in Duncan (1981)'s seminal experimental dataset. This result was achieved by computing the linear-equivalent to the foil-generated breaking waves in the latter experiments.

The present study has two main goals. First, we propose and investigate the validity of a novel linear-equivalent breaking onset criterion, based not only on energy conservation, but also on the conservation of wave impulse. The validation of this criterion is carried out through comparisons with FNPF simulations of focused breaking wave packets, performed with the two-dimensional (2D) model of Grilli et al. (1989) (see also Grilli and Subramanya (1996); Grilli and Horrillo (1997)). The focused wave packets were chosen so as to display a wide range of breaking strengths, characterized by the Γ parameter. These 2D-FNPF simulations are validated through comparison of the free-surface profiles measured in a wave flume for the same cases. Second, we propose an empirical formula, which relates the breaking strength parameter Γ of a wave to its linear equivalent. The validity of the linear-equivalent breaking onset criterion and breaking strength parameter will be investigated for a wide variety of individual focused breaking wave events featuring different levels of breaking strength ($\Gamma \in [0.82; 3.92]$), from mild spilling breakers to strong plunging breakers. A careful comparison of the linear and nonlinear results will show that, in most cases, the wave that breaks is not the fully focused wave, but instead one that is partially focused and breaks earlier and upstream of the theoretical focusing time and location. A monotonic evolution of the breaking strength as a function of the steepness of the particular wave crest that breaks will be observed. As indicated earlier, the magnitude of the slamming force was

found to be closely related to the Γ parameter. As engineers use hydro-aero-servo-elastic solvers that generally rely on linear waves and disregard the effect of the structure on the wave field to estimate the wave slamming loads (see for instance Wienke and Oumeraci (2005); Hansen and Kofoed-Hansen (2017); Ghadirian and Bredmose (2019); Ma et al. (2024)), the current model would allow to predict the occurrence and strength of the breaking events, and thus to estimate the wave impact loads. Besides this, the present results could be used in spectral wave propagation models to estimate the energy dissipated by breaking events. As a first step, the current study is restricted to long-crested breaking waves, although it has been shown that wave directionality affects the breaking process (e.g., McAllister et al., 2019).

The paper is organized as follows. Section 2 presents in details the waves and the wave generation process. The free-surface profiles simulated with the 2D-FNPF model are compared with the experimental profiles. Section 3 presents the wave properties computed based on these nonlinear simulations, including the B and Γ parameters. In Section 4, a linear-equivalent of the breaking onset criterion is derived, by considering a regular wave. The validity of this criterion is assessed in Section 5 for the focused waves. In Section 6, we propose an empirical formula to compute the breaking strength of the focused waves using their linear equivalent. The values obtained with the linear-equivalent criterion are compared to the values obtained with the 2D-FNPF model. Finally, conclusions are drawn in Section 7.

2. Generation and measurement of the breaking waves

In this section, we present the procedure used to generate the different breaking and non-breaking wave packets considered in the work, both in the numerical model and in the laboratory wave flume. Waves are simulated using a 2D-FNPF model, whose results are validated based on experiments carried out in the wave flume of Ifremer, Brest. The flume is 40.5 m long from the wave generator to the absorbing beach, 2 m deep and 4 m wide, and is equipped with a segmented piston-type wavemaker. The flume bottom has a -0.5% slope in the longitudinal and transversal directions. Breaking waves are generated through frequency focusing. They have a wide variety of parameters, in particular in terms of breaking strength. In the following, the breaking location, x_b, is defined as the point at which the wave free-surface profile first reaches a vertical slope and the breaking time, t_b, as the instant at which this event occurs.

2.1. Numerical wave tank modeling and generation of focused breaking waves

A numerical wave tank (NWT) based on 2D-FNPF theory is used to simulate the generation through frequency focusing of several breaking waves in the wave flume of Ifremer. The choice of a potential flow model has been motivated by the ability of such models to accurately propagate waves along important distances (see Paulsen et al. (2014) for instance.) The geometry of the NWT is similar to that of the wave flume, except that it is 45 m long. It was deemed unnecessary to add a numerical absorbing beach at its far end, since the simulation times were sufficiently short, up to t_b, to prevent waves from propagating to the tank far end and back to the breaking location. To verify this, the NWT length was increased to 50 m and no changes in free-surface elevation at the breaking location were observed. In the NWT, at any given time t, FNPF equations are solved with a higher-order boundary element method (BEM), whose results are used to update both the free-surface geometry and boundary conditions to the next time level (Grilli et al., 1989; Grilli and Subramanya, 1996; Grilli and Horrillo, 1997). In the BEM, the boundary of the fluid domain, which consists in the free surface, the wave paddle, the far end of the flume, and the bottom, is discretized using N nodes; higher-order elements are used to interpolate both the geometry and the field variables in between nodes. The discretization, which is detailed in Appendix A, is finer in and around the breaking area, to achieve a more accurate description of the fluid flow close to the breaking point. A convergence study is also presented in Appendix A. Note that the slope of the physical tank is taken into account in the FNPF computations, but not in the linear computations presented in sections 4 and 5. Figure 14 in Appendix A shows that, for wave A7, taking the slope into account leads to a difference of less than 4% on the value of Γ compared to a simulation with a flat bottom (see table 2). For the breaking waves, the computation stops at the instant at which the tongue of the wave impinges the free surface. For the non-breaking waves, the computation is stopped a few seconds after the focalization.

Breaking is obtained using the frequency focusing method of Rapp and Melville (1990), with the focused wave energy spectral density $S(f)$ being a standard JONSWAP spectrum, in which high frequency components are truncated beyond some frequency cut-off f_c to prevent early breaking of shorter waves. The wave focusing method assumes linear wave theory, with the corresponding linear dispersion relationship. Thus, the free-surface elevation, $\eta(x, t)$, at location

x and time t, is defined as:

$$\eta(x,t) = \sum_{m=1}^{M} a_m \cos(k_m x - \omega_m t - \phi_m), \tag{2}$$

in which $a_m = \sqrt{2S(f)\Delta f}$ are the wave constituent amplitudes, k_m their wavenumbers, ϕ_m their phases and $\omega_m = 2\pi f_m$ their angular frequencies. The M constituents of frequency f_m are evenly spaced by Δf over the frequency range $[0, f_c]$. For each constituent, the angular frequency and wavenumber satisfy the so-called linear dispersion relationship:

$$\omega_m^2 = gk_m \tanh(k_m h), \tag{3}$$

in which h is the water depth. To achieve wave focusing, the phases ϕ_m are selected such that the wave constituents all reach their maximum elevation at a focusing location x_f and focusing time t_f, i.e.:

$$\phi_m = k_m x_f - \omega_m t_f. \tag{4}$$

The paddle stroke time series, $s_p(t)$, is then obtained by applying the Biésel transfer function $T(k_m h)$ to the free-surface elevation constituents at $x = 0$, while phase-shifting them by $\pi/2$ (Andersen and Frigaard, 2014):

$$s_p(t) = \sum_{m=1}^{M} \frac{a_m}{T(k_m h)} \sin(\omega_m t + \phi_m). \tag{5}$$

Following Derakhti et al. (2018), we define the linear prediction of the wave packet global steepness as:

$$S_L = \sum_{m=1}^{M} a_m k_m. \tag{6}$$

On this basis, waves of different breaking strengths can be generated by varying the linear steepness, i.e. by varying the amplitude a_m of the wave components. For a JONSWAP spectrum, the latter are calculated using the spectral density:

$$g(f) = \alpha H_s^2 f_p^4 f^{-5} e^{-\frac{5}{4}\left(\frac{f}{f_p}\right)^{-4}} \gamma^b, \tag{7}$$

where

$$b = e^{-\frac{(f-f_p)^2}{2\sigma^2 f_p^2}}, \tag{8}$$

in which $\sigma = 0.07$ if $f < f_p$ and $\sigma = 0.09$ if $f > f_p$, with $f_p = 1/T_p$ denoting the spectral peak frequency. In Eq. (7), the coefficient α is selected such that:

$$H_s^2 = 16 \int_0^{\infty} g(f) \mathrm{d}f. \tag{9}$$

Note that, here, H_s is only used as a parameter of the spectrum and does not represent the significant wave height of a sea state, in which the obtained focused breaking wave would be likely to occur. In the following, the value of parameter H_s was varied to adjust the amplitude of the components and the resulting focused wave characteristics.

To illustrate the influence of S_L on the breaking mechanism, the generation methodology was applied using a particular JONSWAP spectrum with a peak period $T_p = 2.25$ s, peak enhancement factor $\gamma = 3.3$, a cut-off frequency $f_c = 0.8$ Hz, and a frequency resolution $\Delta f = 0.01$ Hz (hence $M = 80$). The depth of the tank being $h = 2$ m, we find $k_p h = 1.70$, which corresponds to an intermediate water depth. The focusing time is set to $t_f = 50$ s and the focal point to $x_f = 21$ m. Based on this spectrum, we generated 9 breaking and non-breaking waves, with a linear steepness in the range $S_L \in [0.286; 0.442]$. The free-surface profiles at the breaking time (or when the wave elevation reaches its maximum for the first two non-breaking wave packets) obtained for different S_L values are shown in Fig. 1. Their simulated breaking times and locations (t_b, x_b), and other parameters, are listed in Table 1. The height of the crest at focusing obtained from linear wave theory, $A = \sum_{n=1}^{N} a_n$, is also provided. Based on the NWT results, the 7 waves that are actually breaking can be classified into three groups, labeled 1, 2 and 3 in Table 1. The breaking group
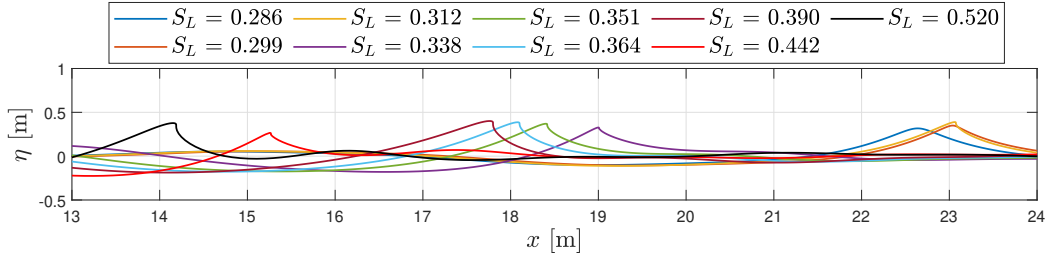
Figure 1: Free-surface profiles of 9 frequency-focused waves of increasing linear steepness S_L simulated in the 2D-FNPF NWT at the time of breaking (or maximum elevation for the first two non-breaking waves $S_L = 0.286$, $S_L = 0.299$). The wave parameters are listed in Table 1.

S_L [1]	$A = \sum\limits_{n=1}^{N} a_n$ [m]	H_s [m]	x_f [m]	t_f [s]	Breaking	Breaking group	x_b [m]	t_b [s]
0.286	0.242	0.11	21	50	No			
0.299	0.253	0.115	21	50	No			
0.312	0.264	0.12	21	50	Yes	1	23.07	50.49
0.338	0.286	0.13	21	50	Yes	2	19.01	47.25
0.351	0.297	0.135	21	50	Yes	2	18.42	46.95
0.364	0.308	0.14	21	50	Yes	2	18.10	46.78
0.390	0.330	0.15	21	50	Yes	2	17.80	46.60
0.442	0.374	0.17	21	50	Yes	3	15.27	44.12
0.520	0.440	0.20	21	50	Yes	3	14.19	43.47

Table 1

Parameters of 9 frequency-focused waves of increasing linear steepness S_L simulated in the NWT (see Fig. 1). Parameters x_f and t_f are respectively the theoretical location and time of focusing given by the linear theory; x_b and t_b are the breaking location and time obtained with the NWT. All simulations are run with $T_p = 2.25$ s, $\gamma = 3.3$, $f_c = 0.8$ Hz and $\Delta f = 0.01$ Hz. Note, here, H_s is only a spectral parameter and not the significant wave height of a sea state in which the focused breaking wave would be likely to occur.

1, composed of only one wave, corresponds to the case where the focused wave breaks. This occurs slightly beyond the theoretical focal point, but close to the theoretical focusing time. In group 2, breaking occurs around $x = 18$ m and $t = 47$ s, and it is no longer the focused wave crests that break, but waves that are only partially focused. For group 3, breaking occurs around $x = 15$ m and $t = 44$ s, and the breaking waves are even less focused than those of group 2. We will show later in Sec. 5 that the breaking group to which a breaking wave belongs can be determined based on linear theory. However, within a given group, the actual breaking location and time are affected by nonlinear effects. We observe in Fig. 1 that, within a given group, an increase of the linear steepness leads to a seemingly more violent breaking event, which occurs earlier in time and space. At some point, further increasing the linear steepness will lead to a much larger shift in both breaking time and location: this corresponds to a change of the wave crest that breaks. It should be noted that, with the different considered wave spectra, we never obtained strong plunging breakers in the breaking group 1 (see Table 1), i.e., when the fully focused wave breaks. The strongest plunging breakers that were obtained corresponded to partially focused waves (breaking groups 2 and 3).

Progressively increasing S_L for the focused wave packets simulated in the NWT allows simulating different breaking wave strengths, but these waves break at different times and locations. For the flume experiments, however, it was necessary that all waves break at about the same location, here set to $x_t = 21$ m. This was achieved by iteratively modifying the theoretical focusing location x_f in the NWT simulations, while keeping $t_f = 50$ s. More specifically, in the iterative NWT simulations, the first iteration, $i = 1$, corresponds to the earlier simulations, i.e., with the focal point set to $x_f = x_t = 21$ m. As shown in Fig. 1, this produces waves that break at various locations, from $x_b = 14.19$
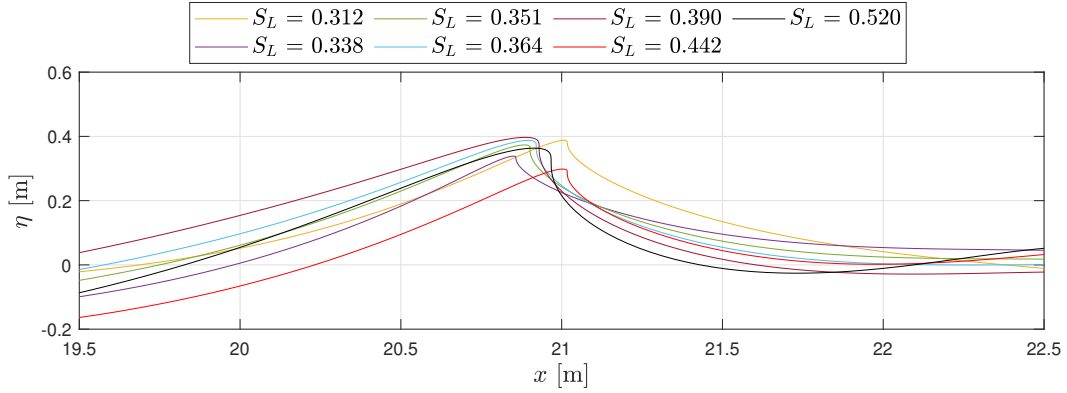
Figure 2: Free-surface profiles of seven frequency-focused breaking waves (groups 1 to 3 in Table 1) at the instant they break in the NWT simulations. Their theoretical focusing location, x_f, was iteratively adjusted (Eq.10) to achieve $x_b \simeq x_t = 21$ m. See parameters listed in Table 2 for waves A3-A9.

to 23.07 m. In subsequent iterations, the theoretical focal point is adjusted as:

$$x_f^{i+1} = x_f^i - (x_b^i - x_t),\qquad(10)$$

where x_b^i is the breaking location observed in the NWT at the ith iteration. Simulations are repeated with the new focal point until a satisfactory convergence to the desired breaking location x_t is reached. For all the simulated cases, only 3 to 4 iterations were required to obtain a breaking location within ± 0.1 m of x_t. Figure 2 shows the converged free-surface profiles of the waves obtained by applying this iterative method to the last seven waves listed in Table 1 (groups 1 to 3). The profiles are shown at the instant of breaking.

The theoretical focusing locations of the frequency-focused breaking waves used in the following were all identified based on NWT simulations, using this iterative method. These are listed in Table 2 along with the spectral parameters. All the focused wave packets have a focusing time $t_f = 50$ s and are based on JONSWAP spectra with a cut-off frequency $f_c = 0.8$ Hz. This cut-off frequency was selected to prevent the spurious breaking of small waves in the model, which would have interrupted simulations before the main breaking event occurred. The waves are divided into two sets of nine waves each, referred to as A and B. For sets A and B, the spectral peak periods are $T_p = 2.25$ and 2.49 s, and the peak enhancement factor are $\gamma = 3.3$ and 1.4, respectively. In each set, the parameter A is varied, through adjusting H_s, to generate waves of different breaking strength. The resulting linear steepness S_L (Eq. 6) of each wave packet is also listed in Table 2.

2.2. Validation of the simulated free-surface profiles with experimental measurements

The focused breaking waves that were simulated in the NWT were generated in the physical flume, by specifying the same stroke time series at the piston wavemaker. The experimental parameters are identical to those listed in Table 2, except that the focusing time is reduced to 30 s. This change is not important since the experimental results are used here to assess the accuracy of the 2D-FNPF NWT simulations. Each experiment was repeated 3 times, after letting the flume rest for 45 minutes in between, to ensure a good repeatability of the breaking waves.

In each experiment, the free-surface elevation of the incident wave packet was measured with a servo-controlled non-intrusive wave gauge (see Ohana and Bourdier (2014) for details of the wave gauge) working at an acquisition rate of 50 kHz and located upstream of the breaking location $x_b \simeq 21$ m, at $x = 11.895$ m. The free-surface profiles of the breaking waves were measured in space along the flume sidewall, with a high-speed video camera centered around the breaking location (Fig. 3). The camera recorded 2000 frames per second. A 2 m long checkerboard, shown in Fig. 3a, was used to carry out the intrinsic and extrinsic calibrations of the video camera. The extrinsic calibration allows to compensate for the varying pixel size resulting from the fact that the optical axis of the camera is not perpendicular to the flume sidewall. The red dots in the figure mark the checkerboard corners detected by the calibration algorithm. These are used to transform the pixel coordinates of a point into its checkerboard coordinates. The flume coordinates are then calculated by applying a rotation and a translation of the checkerboard coordinates, defined using the horizontal

| Number	$A = \sum_{n=1}^{N} a_n$ [m]	H_s [m]	T_p [s]	γ [1]	f_c [Hz]	x_f [m]	t_f [s]	S_L [1]
A1	0.242	0.11	2.25	3.3	0.8	19.37	50	0.286
A2	0.253	0.115	2.25	3.3	0.8	18.97	50	0.299
A3	0.264	0.12	2.25	3.3	0.8	18.80	50	0.312
A4	0.286	0.13	2.25	3.3	0.8	22.99	50	0.338
A5	0.297	0.135	2.25	3.3	0.8	23.57	50	0.351
A6	0.308	0.14	2.25	3.3	0.8	23.87	50	0.364
A7	0.330	0.15	2.25	3.3	0.8	24.15	50	0.389
A8	0.374	0.17	2.25	3.3	0.8	27.04	50	0.442
A9	0.440	0.20	2.25	3.3	0.8	27.16	50	0.520
B1	0.259	0.11	2.49	1.4	0.8	19.47	50	0.289
B2	0.282	0.12	2.49	1.4	0.8	18.84	50	0.315
B3	0.306	0.13	2.49	1.4	0.8	19.69	50	0.341
B4	0.329	0.14	2.49	1.4	0.8	23.42	50	0.368
B5	0.353	0.15	2.49	1.4	0.8	23.92	50	0.394
B6	0.376	0.16	2.49	1.4	0.8	24.08	50	0.420
B7	0.400	0.17	2.49	1.4	0.8	23.94	50	0.447
B8	0.423	0.18	2.49	1.4	0.8	23.72	50	0.473
B9	0.447	0.19	2.49	1.4	0.8	26.05	50	0.499

Table 2
Parameters of breaking and non-breaking waves simulated in the NWT based on JONSWAP spectra: theoretical crest elevation A at focusing based on linear wave theory, peak period T_p, peak enhancement factor γ, and cut-off frequency f_c. Parameters x_f and t_f are the focus location and time based on linear wave theory, which are such that waves break at $x_b \simeq 21$ m in the NWT; S_L denotes the linear steepness of the focused wave packet (Eq. 6).

datum represented by the still water line and a reference mark located 21 m away from the wave paddle. Figure 3b illustrates the detection of the free-surface profile at the wall using a Canny-type contour detection algorithm. The blue dots mark the pixels at the intersection between the free surface and the tank wall. The contour detection algorithm is applied on the image located between the two red lines shown in the figure. The transformation obtained from the linear calibration is applied to transform the pixel coordinates of the free surface into the flume coordinates. More details on the measurement methodology can be found in Hulin (2024).

Figure 4a shows time series of free-surface elevations measured with the wave gauge, for three replicates of one focused wave experiment (similar to A6, except for $t_f = 30$ s), together with the corresponding NWT simulation (also for $t_f = 30$ s). At this scale, the agreement between the different runs and the numerical simulations is excellent. The zoomed-in view of the same data in Fig. 4b shows that differences in surface elevation between the experimental replicates are small, on the order of 1 mm. Differences between the experimental results and the numerical simulations are slightly larger, ~ 3 mm. A time shift of ~ 20 ms is also observed.

Figure 5 shows free-surface profiles measured near the breaking zone at different times for the three experimental replicates of this wave, together with the profiles simulated in the NWT. The different experimental curves agree very well with each other. Except for a small time/phase shift, the agreement between the numerical and experimental profiles is quite good, all the way to the breaking location. Differences between the numerical and experimental curves, however, seem to be increasing as the wave approaches breaking, with the experimental wave crest elevation being slightly smaller. Since free-surface profiles are measured along the flume sidewall with the video camera, this mild wave damping could result from viscous dissipation in the wall boundary layer, which is not represented in potential flow theory. Hence, as noted by Rapp and Melville (1990), the fluid kinematics, and waves, may be slightly different, and less affected by sidewall friction, in the middle of the flume. In particular, it was reported in the latter work that breaking occurred earlier at the wall. Similar comparisons between experimental and NWT results were performed for other waves, whose details are given in Appendix B.
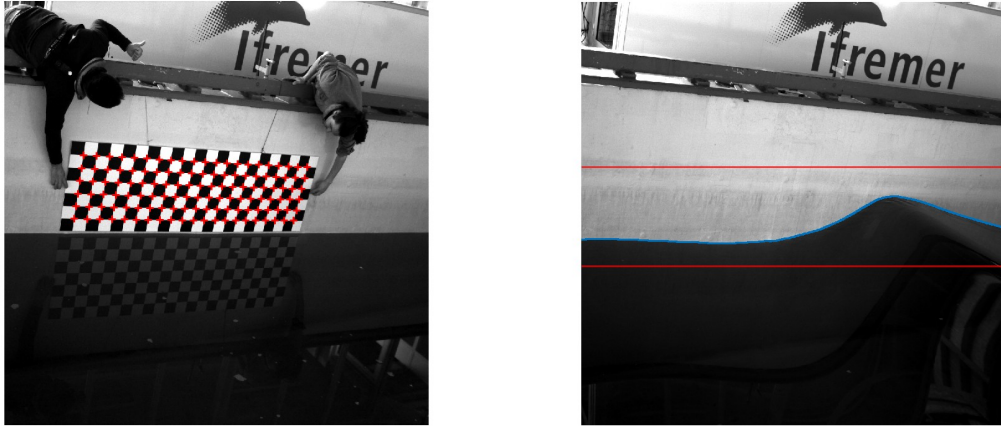
(a) Checkerboard placed on the flume sidewall for calibration. Red dots mark detected checkerboard vertices.

(b) Free-surface measurement using a contour detection algorithm (applied to the image between the two red lines to avoid detecting spurious contours). Blue dots mark detected free-surface points.

Figure 3: Wave free-surface profile measurement using a high-speed video camera.

(a)

(b)
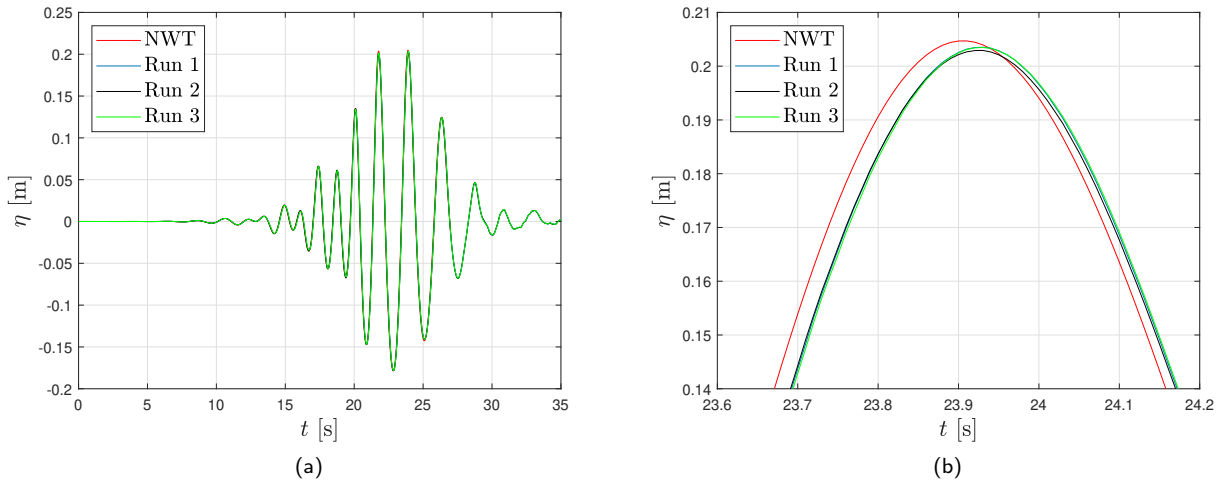
Figure 4: (a) Time series of free-surface elevation measured at the wave gauge located at $x = 11.895$ m for three replicates of the same focused wave experiment (similar to A6 except for $t_f = 30$ s). The free-surface elevation simulated with the NWT for the same wave is also shown. (b) Zoomed-in view around the maximum crest of (a).

3. Computation of nonlinear breaking wave parameters from NWT simulations

While accurate and repeatable, the wave flume experiments and the available instrumentation do not allow for a direct and non-intrusive measurement of the fluid particle velocity near and at the crest. It is also quite challenging to accurately measure the wave crest speed in the flume. Both of these measurements are required to compute the breaking onset criterion B. For these reasons, considering their experimental validation, the NWT results are used to estimate the different parameters required to compute the breaking onset criterion B and the breaking strength parameter Γ, defined
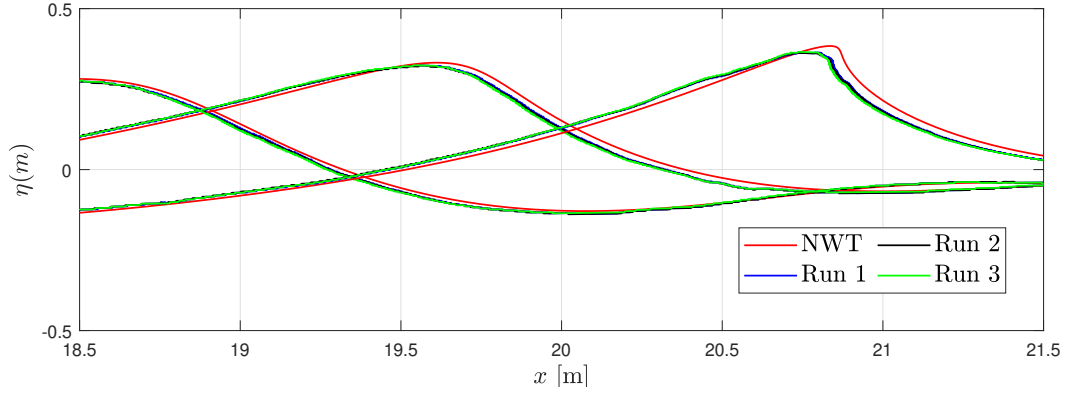
Figure 5: Comparison of simulated (NWT) and experimental free-surface profiles of a wave (similar to A6 except for $t_f = 30$ s) at different times. Runs 1-3 are three replicates of the same experiment.

Number	x_b [m]	t_b [s]	η_b [m]	c [m/s]	Γ [1]	$\frac{dB}{dt}$ [s^{-1}]	Breaking group
A1	20.99	50.42	0.32	2.39			
A2	20.99	50.55	0.35	2.39			
A3	21.01	50.56	0.39	2.72	0.93	0.55	1
A4	20.86	47.17	0.34	2.55	0.82	0.52	2
A5	20.90	46.89	0.37	2.74	1.21	0.69	2
A6	20.92	46.74	0.39	2.82	1.67	0.91	2
A7	20.93	46.56	0.40	2.89	2.78	1.47	2
A8	21.02	43.89	0.30	2.54	1.15	0.71	3
A9	20.97	43.63	0.36	2.92	2.97	1.57	3
B1	20.99	50.39	0.33	2.44			
B2	21.05	50.57	0.41	2.76	0.92	0.53	1
B3	21.00	50.1	0.41	2.86	1.90	1.01	1
B4	20.95	46.97	0.35	2.64	1.06	0.63	2
B5	20.99	46.70	0.39	2.84	1.90	1.02	2
B6	21.02	46.59	0.41	2.93	2.89	1.51	2
B7	20.92	46.55	0.41	3.00	3.70	1.94	2
B8	20.90	46.57	0.41	3.39	3.92	2.15	2
B9	20.99	44.30	0.32	2.34	1.44	0.96	3

Table 3
Parameters of two sets of breaking and non-breaking waves simulated in the NWT based on JONSWAP spectra (see Table 2). Breaking wave parameters are computed at the breaking time t_b. For the non-breaking waves, parameters are computed at the instant at which the free-surface elevation is maximum. See section 2.1 for the definition of the breaking groups.

in Eq. 1. As proposed in earlier work (Barthelemy et al., 2018; Derakhti et al., 2018), this parameter is calculated at the breaking onset threshold $B = u/c = 0.85$, beyond which a wave will inevitably evolve towards breaking.

In the computation of B, the crest celerity is calculated as $c = dx_c/dt$, based on the time history of the crest location in the model simulations, $x_c(t)$ (i.e., the location at which the free surface is maximum). To prevent an oscillatory behavior of the crest celerity, and hence of B, a careful computation of the crest location is required. Generally, $x_c(t)$ is located in between two discretization nodes. For this value to be accurate, a smooth local approximation of the wave crest geometry must be defined (e.g., Mohanlal et al., 2023). To do so, at each time step, the BEM node of maximum surface elevation is first selected: $\mathbf{x}_J$ (where J corresponds to the index of this node). Then, a local cubic smoothing spline approximation of the free surface is made, using 10 nodes of coordinates $\mathbf{x}_j = (x_j, z_j)$ on either side of J, i.e., in the interval $j \in [J - 10; J + 10]$. Similar to the so-called quasi-spline method introduced by Grilli and

Subramanya (1996) in the NWT, this approximation allows for multiple-valued free-surface elevations (such as occurs in overturning waves), by defining two spline approximations of each free-surface coordinate as a function of the node index j: $X(j)$ and $Z(j)$, respectively. Specifically, here, functions X and Z are found by minimizing the following quantity:

$$\sum_{j=J-10}^{J+10} |f_j - F(j)|^2 + (1-p) \int_{J-10}^{J+10} \left| \frac{d^2 F}{dl^2}(l) \right|^2 dl, \tag{11}$$

where $p = 0.8$ is the smoothing parameter, F corresponds to X or Z and f_j corresponds to x_j or z_j, the set of nodal coordinates in the considered interval. Note that this analysis is done in postprocessing, using the Matlab software function `csaps`.

Functions $X(j)$ and $Z(j)$ describe the free surface as a smooth parametric curve with $x = X(j)$ and $z = Z(j)$ from which we identify the x-coordinate of the crest $x_c(t) = X(j_{max})$ and the crest elevation $\eta_c(t) = Z(j_{max})$, where j_{max} is the real value of the curve parameter corresponding to the point of maximum elevation. The crest velocity is then obtained by differentiating the wave crest position with respect to time using a first-order finite-difference scheme. The procedure used here for the computation of the crest location allows to obtain a smooth time evolution that can be directly differentiated numerically without inducing strong oscillations of the crest speed.

Computing B and its time derivative also requires accurately computing the horizontal fluid velocity at the crest. This is done, as for the crest speed, within a local smooth cubic spline approximation of the free surface horizontal fluid velocity, $U(j)$. The latter is similarly obtained by minimizing Eq. 11 with $f_j = u_j$, where u_j are the horizontal velocities computed at the BEM nodes at each time step. The horizontal velocity at the crest is then found as $u(t) = U(j_{max})$.

Figures 6a and 6b show the time evolution of the crest and horizontal fluid velocities computed for waves A3 and A7, respectively. Figure 7a and 7b show the time evolution of B for the same cases. As suggested by Derakhti et al. (2018), the time derivative of B, used to compute Γ, was calculated as the slope of a linear interpolation of $B(t)$ over the time interval during which $|B - 0.85| < 0.03$. This interpolation corresponds to the orange line in Figs. 7a and 7b.

Derakhti et al. (2018) proposed a definition of the characteristic breaking wave period T_b, which they used to compute Γ with Eq. 1. In their work, T_b was calculated based on the linear dispersion relationship, using the wavelength L_b computed at breaking, defined from two successive zero-crossing points around the crest. However, in our simulations of wave sets A and B in the NWT, we observed that in a few cases the forward trough of the breaking wave was above the Still Water Level (SWL) and, therefore, L_b was overestimated by the zero-crossing approach. Accordingly, in the current work, we modified Derakhti et al. (2018)'s definition of T_b to use, instead, the crest velocity computed at breaking onset (when $B(t) = 0.85$), c, together with the linear dispersion relationship (Eq. 3), as:

$$c = \sqrt{\frac{g}{k_b} \tanh k_b h} \quad \text{and} \quad T_b = \frac{2\pi}{\sqrt{g k_b \tanh k_b h}}. \tag{12}$$

Given c, the first equation is used to compute the value of the wavenumber at breaking onset, $k_b = 2\pi/L_b$, and the characteristic wave period T_b is then found from the second equation. Values of the breaking location x_b, breaking time t_b, crest elevation at breaking η_b, crest velocity at breaking c_b, breaking strength Γ, and the time derivative of B at $B = 0.85$ are given in Table 3 for all the focused wave cases.

4. A linear-equivalent breaking onset criterion

In this section, we derive a linear-equivalent breaking onset criterion which aims at predicting the value of u/c from linear wave theory. The approach relies on the definition of a linear wave, which has a mechanical energy and impulse similar to the fully nonlinear wave. In order to do so, we must assume that the wave is regular, but we will explain later (in Section 5) how we suggest to use this approach for irregular waves.

4.1. Definition of the linear-equivalent periodic wave

Given a nonlinear periodic wave, the linear-equivalent wave is defined such that it has the same period-averaged energy E and impulse I, as the nonlinear wave. Once the linear-equivalent wave parameters are calculated, the ratio u/c of the linear-equivalent wave is calculated at its crest and compared to the value found for the nonlinear wave, in order to establish an equivalence. Thus, given the free-surface elevation of a periodic linear (infinitesimally small) wave:

$$\mathring{\eta}(x,t) = \mathring{a} \cos \left(\mathring{k}x - \mathring{\omega}t \right), \tag{13}$$
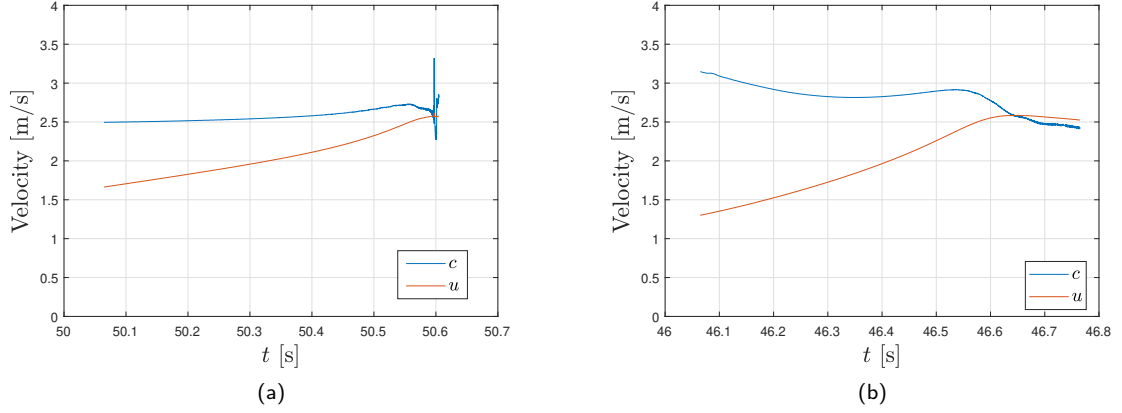
Figure 6: Time evolution of the crest velocity and of the horizontal fluid velocity at the crest for waves A3 (*a*) and A7 (*b*) (see Table 3).
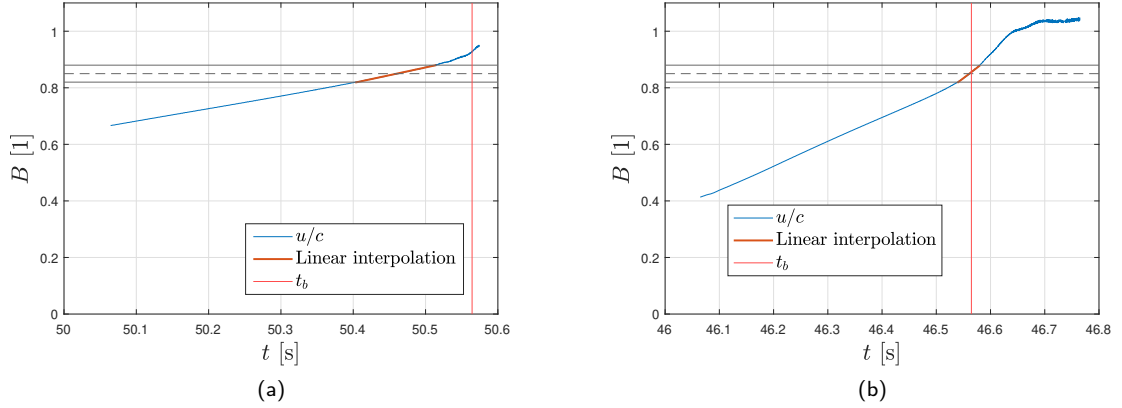

Figure 7: Time evolution of the parameter B for the waves A3 (*a*) and A7 (*b*). The vertical red line corresponds to the breaking time t_b (see Table 3). The dashed horizontal line corresponds to $B = 0.85$ and the two solid horizontal lines to $B = 0.85 \pm 0.03$. As suggested by Derakhti et al. (2018), the linear interpolation is carried out between these two solid horizontal lines.

where the ring symbol " $\overset{\circ}{\cdot}$ " refers to linear-equivalent quantities, a standard second-order perturbation approach (Phillips, 1966) yields the period-averaged potential energy, $\overset{\circ}{E}_p$, and kinetic energy, $\overset{\circ}{E}_k$ as:

$$\overset{\circ}{E}_p = \overset{\circ}{E}_k = \frac{1}{4}\overset{\circ}{a}^2, \tag{14}$$

where, for simplicity, we have assumed that the gravity $g = 1$ and the fluid density $\rho = 1$, without loss of generality since, in the following analysis, we will consider the ratios of the linear and nonlinear quantities. The relationship between the kinetic energy, E_k, and the impulse, I, for a purely progressive wave (linear or nonlinear) is defined by the wave speed $c = \omega/k$ (see Phillips, 1966):

$$I = \frac{2E_k}{c}, \quad \overset{\circ}{I} = \frac{2\overset{\circ}{E}_k}{\overset{\circ}{c}}. \tag{15}$$

Now, enforcing the condition that the linear-equivalent wave has the same total energy, $E = E_p + E_k$, and impulse as the nonlinear wave yields the amplitude and phase speed of the linear-equivalent wave, as:

$$\begin{cases} E = \mathring{E} = \dfrac{1}{2}\mathring{a}^2 \\ I = \mathring{I} = \dfrac{2\mathring{E}_k}{\mathring{c}} = \dfrac{\mathring{E}}{\mathring{c}} = \dfrac{E}{\mathring{c}} \end{cases} \Rightarrow \begin{cases} \mathring{a} = \sqrt{2E} \\ \mathring{c} = \dfrac{E}{I} \end{cases}. \tag{16}$$

Linear-equivalent u/c at the wave crest

The horizontal velocity at the crest of a linear wave, $\mathring{u}$, is (without applying any stretching):

$$\mathring{u} = \frac{\mathring{a}\mathring{k}}{\mathring{\omega}} = \frac{\mathring{a}}{\mathring{c}}. \tag{17}$$

Substituting Eq. 17 into Eq. 16, yields the linear-equivalent $\mathring{B}$ ratio, as a function of the impulse and total energy of the nonlinear wave, as:

$$\mathring{B} = \frac{\mathring{u}}{\mathring{c}} = \frac{\mathring{a}}{\mathring{c}^2} = \frac{I^2}{E^2}\sqrt{2E}, \tag{18}$$

which can also be expressed as a function of the non-dimensional energy, $\widetilde{E} = k^2 E$, and impulse, $\widetilde{I} = k^{3/2} I$, as:

$$\mathring{B} = \frac{\widetilde{I}^2}{\widetilde{E}^2}\sqrt{2\widetilde{E}}. \tag{19}$$

Note, however, that the relative water depth of the linear-equivalent wave, $\mathring{k}h$, which is different from that of the nonlinear wave, is not defined at this stage.

Relative water depth of the linear-equivalent wave

The relative water depth of the linear-equivalent wave may be found using the linear dispersion relation $\mathring{k}\mathring{c}^2 = \tanh\left(\mathring{k}h\right)$ and substituting Eq. 16 into the dispersion relationship:

$$\begin{cases} \mathring{c}^2 = h\dfrac{\tanh\left(\mathring{k}h\right)}{\mathring{k}h} \\ \mathring{c} = \dfrac{E}{I} \end{cases} \Rightarrow \left(\frac{\widetilde{E}}{\widetilde{I}}\right)^2 = kh\frac{\tanh\left(\mathring{k}h\right)}{\mathring{k}h}. \tag{20}$$

Then, given $\widetilde{E}$, $\widetilde{I}$ and a relative water depth kh, solving Eq. 20 gives the linear-equivalent relative water depth $\mathring{k}h$ which will be used in the following. Equation 16 leads to $\mathring{c} < c$ and Eq. 20 to $\mathring{k} < k$. Note that Eq. 20 can lead to nonphysical small values of $\mathring{k}$ compared to k when kh is too small. In the following, the wavelength of the non-linear wave will be assumed to be smaller than 6 times the water depth.

4.2. Relationship between $\mathring{u}/\mathring{c}$ and u/c

Let us now examine the behavior of the linear and nonlinear ratios, $\mathring{B} = \mathring{u}/\mathring{c}$ and $B = u/c$, for different (regular) wave parameters. For this purpose, we use the method of Cokelet (1977), which allows to compute different non-dimensional quantities such as the energy, $\widetilde{E}$, and the impulse, $\widetilde{I}$, for a given nonlinearity level $\epsilon \in [0, 1]$ and a relative water depth parameter $\exp(-kh)$. These quantities can be computed up to the breaking limit $\epsilon = 1$. The nonlinearity level ϵ, also called the expansion parameter, is defined by the equation $\epsilon^2 = 1 - q_{\text{crest}}^2 q_{\text{trough}}^2/c^4$, with q_{crest} and q_{trough} the nonlinear horizontal fluid velocities at the crest and the trough, respectively, in a frame of reference moving at speed c. Note that the numerical values of the horizontal velocity at the crest (not given in Cokelet (1977)) were computed in the present study using the same method. Also note that other approaches could have been used to compute the nonlinear values of u/c (e.g., Clamond and Dutykh, 2018).

For a given relative water depth, B and $\mathring{B}$ only depend on the nonlinearity parameter. As an illustration, Fig. 8a. shows the evolution of B and $\mathring{B}$ as a function of ϵ^2, for an infinite water depth. It can be observed that the linear equivalent $\mathring{B}$ goes through a slight maximum around $\epsilon^2 = 0.92$, similar to what was observed in Cokelet (1977) for the evolution of the energy, impulse, and wave speed parameters. The maximum value of $\mathring{B}$ observed in Fig. 8a corresponds
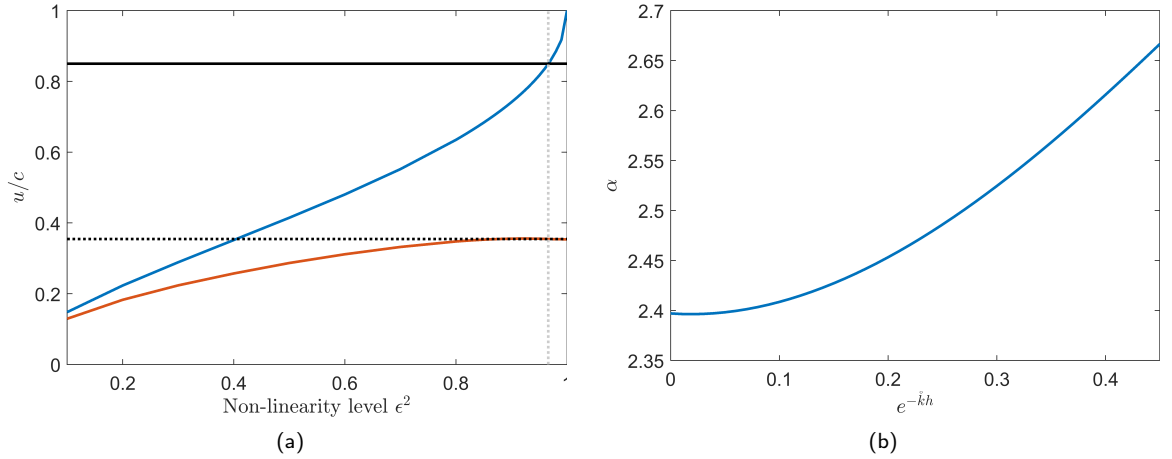
Figure 8: Illustration of the definition of the linear breaking onset criterion. (a) Evolution of the ratio u/c for a nonlinear regular wave (—) and the corresponding equivalent linear wave $\mathring{u}/\mathring{c}$ (—) as a function of the nonlinearity level ϵ^2 for an infinite water depth. The linear breaking onset threshold is defined as the value of $\mathring{u}/\mathring{c}$ for the value of ϵ^2 at which $u/c=0.85$ (—). (b) Evolution of the transfer coefficient $\alpha = 0.85/\mathring{B}_t$ as a function of the relative water depth parameter.

to a nonlinear $B = 0.77$. Based on these observations, we do not find a strict one-to-one correspondence between B and $\mathring{B}$. To simplify the problem and, as we are interested in predicting when the nonlinear wave up-crosses $B = 0.85$, we suggest to use the value $\mathring{B}_t = \mathring{B}(\epsilon^2)$ corresponding to $B(\epsilon^2) = 0.85$ for the detection of the breaking onset. After computing the ratio $\alpha = 0.85/\mathring{B}_t$ for any relative water depth parameter, $\mathring{k}h$, we define the linear-equivalent breaking onset threshold of a nonlinear periodic wave as:

$$\alpha\left(\mathring{k}h\right)\mathring{B} > 0.85. \tag{21}$$

The evolution of α as a function of the linear relative water depth $\mathring{k}h$ is plotted in Fig. 8b, for the range of water depths within which the linear-equivalent model is expected to be valid. In this range, the transfer function α may be approximated by the following expression:

$$\alpha\left(\mathring{k}h\right) \approx \frac{0.85}{0.3546 + 0.0113\,e^{-\mathring{k}h} - 0.3056\,e^{-2\mathring{k}h} + 0.2298\,e^{-3\mathring{k}h}}. \tag{22}$$

5. Wave breaking prediction using the linear breaking onset threshold

In this section, we assess whether the linear-equivalent breaking onset criterion derived in Section 4 can accurately predict the breaking of the focused wave packets presented in Section 3. For this purpose, we assume that the free surface of the linear-equivalent wave is defined by Eq. 2 and that the horizontal fluid velocity at the free surface of the linear-equivalent wave is given by the corresponding linear wave kinematics:

$$\mathring{u}(x,t) = \sum_{m=1}^{M} a_m \frac{gk_m}{\omega_m} \cos\left(k_m x - \omega_m t - \phi_m\right), \tag{23}$$

where the amplitudes, angular frequencies, wavenumbers and phases correspond to those used in Eqs. 2 and 4. The wave crest speed is calculated from the second derivatives of the free-surface elevation η_{xt} and η_{xx} using the following equation (see Longuet-Higgins (1957), Equation 2.5.18):

$$\mathring{c}(t) = -\frac{\eta_{xt}\left(x_{max}(t),t\right)}{\eta_{xx}\left(x_{max}(t),t\right)}, \tag{24}$$

with $x_{max}(t)$ the position of the wave crest that has the largest value of $\mathring{B}$ and, as a consequence, is most likely to break. Once the crest speed is computed, the instantaneous relative water depth is computed using the linear dispersion relationship. As will be shown later, the linear breaking onset criterion in Eq. 21 predicts the breaking onset quite well. However, a better agreement is obtained with the following slightly modified breaking onset criterion:

$$\overline{B} = 1.04 \times \alpha \left(\mathring{k} h \right) \mathring{B} > 0.85. \tag{25}$$

Note that the factor 1.04 was determined empirically such as to obtain a better agreement with the present numerical results, but discriminating a very mild spiller from a non-breaking steep wave may remain difficult when using this linear-equivalent criterion.

Figure 9 shows the evolution of $\overline{B}$ as a function of time for the different wave cases defined in Table 3. The solid lines correspond to the early stage, during which $\overline{B}$ remains below 0.85 and, after the first up-crossing of this threshold, the evolution of $\overline{B}$ is represented by dotted lines. The colored bullets mark the time, t_b, at which the wave starts breaking in the FNPF-NWT, i.e. when the wave profile presents a vertical tangent for the first time. In the wave set A (Fig. 9a), we see that cases A1 and A2 do not up-cross the threshold $\overline{B} = 0.85$ and the waves do not break in the numerical simulations, while this threshold is up-crossed for case A3 and the wave breaks close to the focusing time in the NWT simulations. Waves in cases A4 to A7 also up-cross the 0.85 threshold close to the focusing time, but they had already up-crossed the threshold 4 seconds earlier than for case A3, which indicates that these waves break approximately 4 seconds earlier than the wave of case A3. This is confirmed by the NWT simulations, which also predict the breaking of these waves approximately 3 seconds earlier than for case A3 (see Table 3). For cases A8 and A9, the linear-equivalent breaking threshold $\bar{B} = 0.85$ is up-crossed 8 s before the focusing time. This earlier breaking is confirmed by the NWT simulations. For the wave set B (Fig. 9b), no breaking occurs in the wave packet B1, while breaking occurs close to the focusing time for cases B2 and B3. For cases B4 to B8, parameter $\overline{B}$ reaches a value of 0.85 approximately 4 seconds before the focusing time, which is a good prediction of the earlier breaking also observed in the NWT simulations. However, for case B9, the threshold value is reached after breaking has occurred in the NWT simulations, although a rather large value of $\overline{B}$ (just below 0.85) is reached at $t \approx 42.5$ s. This may show some limitations of the approach, which may not be able to distinguish breaking waves from non-breaking waves when the breaking strength is very small. Nevertheless, these results indicate that the parameter $\overline{B}$ is overall very good at predicting which wave crest is breaking. These results suggest that the waves break earlier than the focusing time because, as a result of wave component superposition in the focusing train, the threshold $\overline{B} = 0.85$ is up-crossed much earlier than the focusing time, and not because the celerity of the waves is affected by local nonlinearity. Indeed, nonlinearity only causes a moderate increase of the wave phase speed, due to amplitude dispersion, that cannot explain the large difference in breaking time for only slightly different wave packets (e.g., A3 compared to A4).
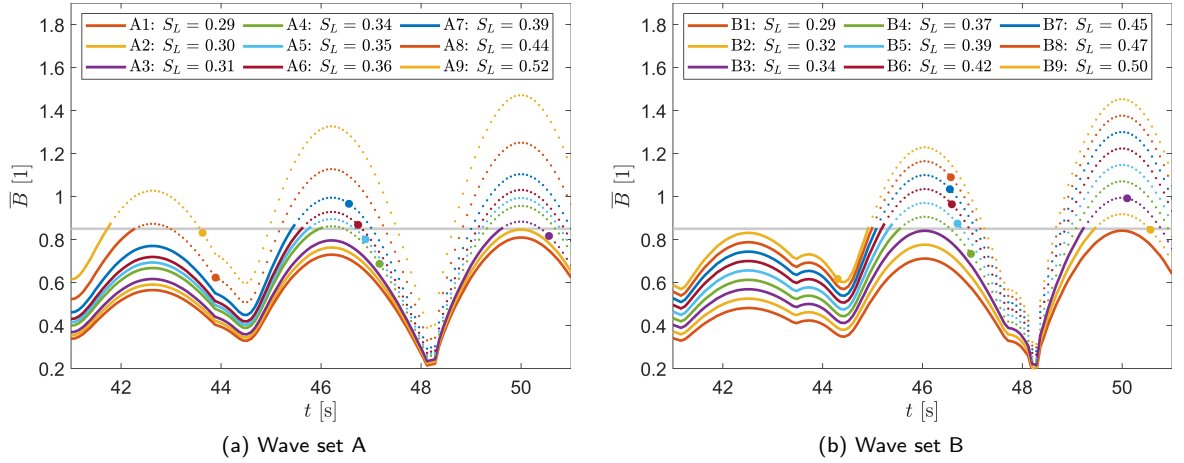
Figure 9: Evolution of the predicted breaking parameter $\overline{B}$ as a function of time. Lines are dotted after the first up-crossing of the level 0.85 and the dots represent the instant of breaking in the FNPF simulations.

6. Breaking strength prediction

In this section, we analyze the ability of parameter $\overline{B}$, obtained from linear-equivalent characteristics, to predict the breaking strength parameter $\Gamma = T_b \, \mathrm{d}B/\mathrm{d}t$. For this purpose, let us examine the evolution of B and $\overline{B}$ depicted in Fig. 10 for two wave cases. The evolution of B is only represented in the neighborhood of $B = 0.85$, as Γ relies on the time derivative of B at this instant. Note that the value $\overline{B} = 0.85$ is reached before the instant corresponding to $B = 0.85$. In addition, one can clearly see that the slopes of $\overline{B}$ and B are different. This may be explained by the fact that $\overline{B}$ was derived from the ratio between B and $\mathring{B}$ when $B = 0.85$, but this ratio is different for other values of B. However, the values of Γ and $\mathring{T}_b \, \mathrm{d}\overline{B}/\mathrm{d}t$ computed for the different wave cases considered in the previous sections present a good correlation, as shown in Fig. 11. This suggests that the breaking strength of the waves may be well predicted using the following equivalent parameter:

$$\overline{\Gamma} = 3.89 \, \mathring{T}_b \, \frac{\mathrm{d}\overline{B}}{\mathrm{d}t}, \tag{26}$$

where the factor 3.89 was derived from the correlation coefficient identified from the data presented in Fig. 11.

One may expect the breaking strength to be related to the linear global steepness of the wave packet, S_L, as defined in Eq. 6. Derakhti et al. (2018) observed that focused wave packets, which were generated using a different wave spectrum from the ones considered in our study, were not breaking for $S_L = 0.3005$ and breaking for $S_L = 0.302$. Here, we find that the wave packets contain a breaking wave when $S_L > 0.3$. The results presented in (Derakhti et al. (2018), Table 1, cases A3-A6) may suggest that the breaking strength is increasing with the global steepness of the wave packet. However, Fig. 12a shows that, for all the waves of sets A and B that break, the evolution of the breaking strength is non-monotonic as we increase the steepness of the wave packet, S_L. This can be explained by the fact that S_L is representative of the steepness of the perfectly focused waves, but not of the local steepness of the wave crests which break prior to the focusing time (imperfectly focused waves). The local steepness of the particular wave crest which breaks may also be estimated from linear wave theory by considering the product, $k\eta_c$, with k a wave number defined according to the shape of the wave crest and η_c the crest elevation of the wave when it passes through its maximum. For this particular analysis, the wave number, k, was computed based on the definition of Derakhti et al. (2018) for the sake of comparison. Figure 12b shows that the breaking strength evolves linearly with the local linear steepness, $k\eta_c$. In addition, we find that $k\eta_c = 0.29$ is also a valid threshold to predict the breaking of the wave crests which break prior to the focusing time.
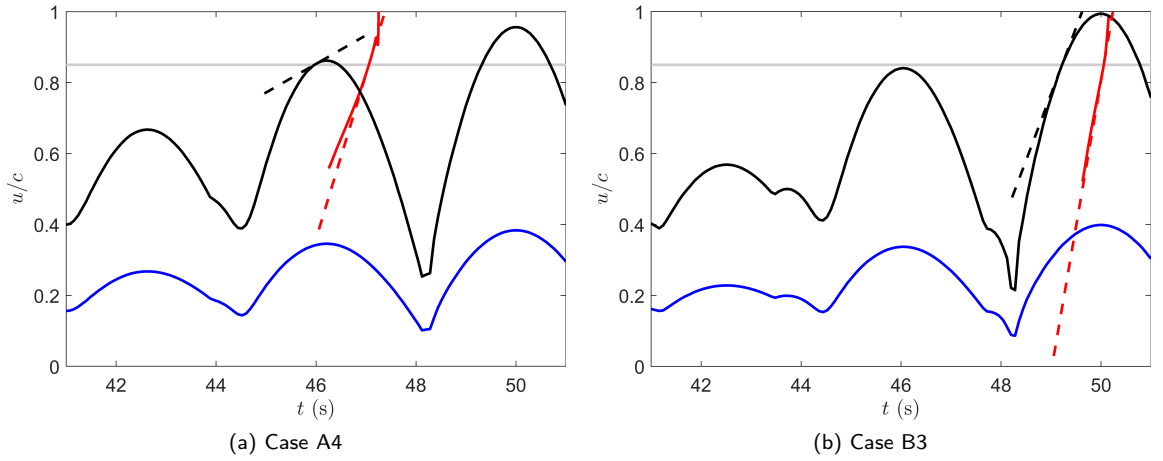
Figure 10: Time evolution of $\mathring{B}$ (—), $\bar{B}$ (—) and B (—) for the wave cases A4 (a) and B3 (b). Comparison of the slopes $\mathrm{d}\bar{B}/\mathrm{d}t$ (--) and $\mathrm{d}B/\mathrm{d}t$ (--) used to calculate $\bar{\Gamma}$ and Γ.
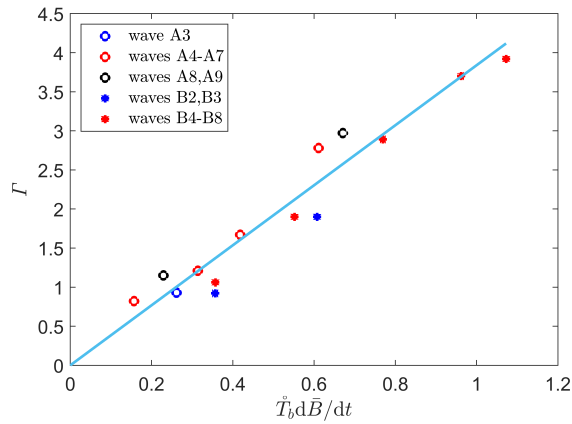

Figure 11: Evolution of the nonlinear breaking strength parameter Γ (derived from the FNPF simulations) as a function of the linear estimate $\mathring{T}_b\mathrm{d}\bar{B}/\mathrm{d}t$. The waves of set A are marked with circles and that of set B with stars. The different colors correspond to the breaking groups given in Table 3: blue for group 1, red for group 2 and black for group 3.
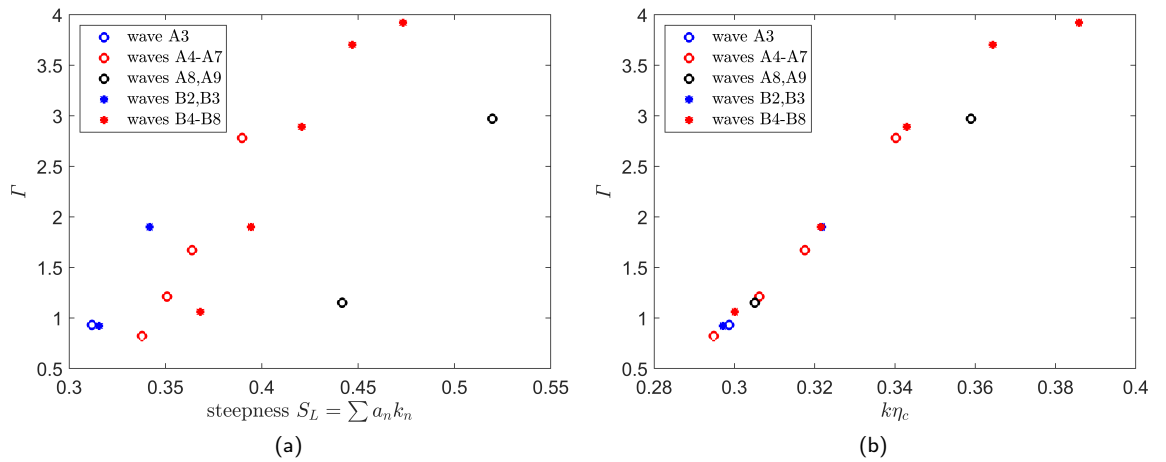
Figure 12: Evolution of the nonlinear breaking strength Γ as a function (a) of the linear wave steepness S_L of the focused wave and (b) of the linear steepness of the breaking wave crest $k\eta_c$. The waves of set A are marked with circles and that of set B with stars. The different colors correspond to the breaking groups given in Table 3: blue for group 1, red for group 2 and black for group 3.

7. Conclusions

In this paper, we showed that the breaking onset and the breaking strength parameters of nonlinear waves could be estimated using linear wave models and we derived predictive equations to do so. Our findings are important as they allow identifying both waves that break and how intense breaking is in time series of focused wave packets generated by standard linear superposition methods. As this approach requires only a modest computational effort, in comparison to running FNPF or CFD models, our methodology will allow easily simulating statistically meaningful sets of breaking waves and, based on these, performing probabilistic analyses of wave breaking, and of the characteristics of breaking waves, in various sea states.

Specifically, building on the work of Barthelemy et al. (2018), who proposed a universal breaking onset criterion, $B = u/c > 0.85$, we developed a linear-equivalent breaking onset criterion, based on the characteristics of an equivalent linear wave that has the same energy and impulse as a regular nonlinear wave. Our method improves the earlier work of Stringari et al. (2021), who only considered the conservation of energy.

We assessed the predictive ability of the linear-equivalent breaking onset criterion by performing simulations of 18 breaking and non-breaking focused waves in a 2D-FNPF-NWT. Although already well-validated experimentally in earlier work, we performed a specific validation of the NWT against experiments in a laboratory flume run for some of the same focused breaking waves, and found a very good agreement of the simulated free-surface profiles with experimental results, up to the breaking point (vertical tangent on the wave front face). Based on the NWT results, we found that, after applying a nearly unity correction factor (1.04) to its theoretical value, the linear-equivalent breaking criterion could predict breaking onset with good accuracy, for the focused wave cases studied here, which covered a fairly wide range of steepness/breaking strength.

In addition, we showed that the breaking strength of the waves computed in the NWT, expressed as parameter Γ proposed by Derakhti et al. (2018), could also be accurately predicted based on a linear-equivalent wave model, using a simple constant correlation factor.

One caveat in our study is that these encouraging results were obtained considering only a specific set of unidirectional waves, whose energy was distributed as a JONSWAP spectrum, and for which breaking resulted from frequency focusing. Hence, in future work, the proposed linear-equivalent breaking onset criterion and strength parameter should be validated for a wider range of wave conditions (relative water depth, wave spectrum, directional spreading, value of the phases at focusing). In particular, the more realistic case of irregular breaking waves should be considered. If these additional validations confirmed the universality of the present findings, further important scientific developments could result in the field of breaking occurrence statistics and strength, which are key to a wide range of marine geophysics and ocean engineering applications.

An additional limitation of the present work is that the effect of a structure on the wave field is not taken into account in the simulations. Indeed, the diffracted and radiated waves around the structure will modify the incident wave field and, hence, are likely to affect the occurrence and characteristics of breaking waves. This limitation could be addressed in future work, by computing the first-order diffraction and radiation terms and by accounting for these terms in the computation of the B and Γ parameter. This would however require a dedicated validation.

CRediT authorship contribution statement

Florian Hulin: Conceptualization, Methodology, Software, Validation, Formal analysis, Investigation, Writing - Original Draft. **Marc Prevosto:** Conceptualization, Methodology, Validation, Formal analysis, Investigation, Writing - Original Draft. **Alan Tassin:** Conceptualization, Methodology, Writing - Original Draft, Writing - Review & Editing, Supervision. **Jean-François Filipot:** Conceptualization, Methodology, Writing - Original Draft, Writing - Review & Editing, Supervision, Project administration, Funding acquisition. **Nicolas Jacques:** Conceptualization, Writing - Original Draft, Writing - Review & Editing, Supervision. **Stephan Grilli:** Software, Resources, Writing - Review & Editing.

Declaration of competing interest

The authors declare that they have no known competing financial interests or personal relationships that could have appeared to influence the work reported in this paper.
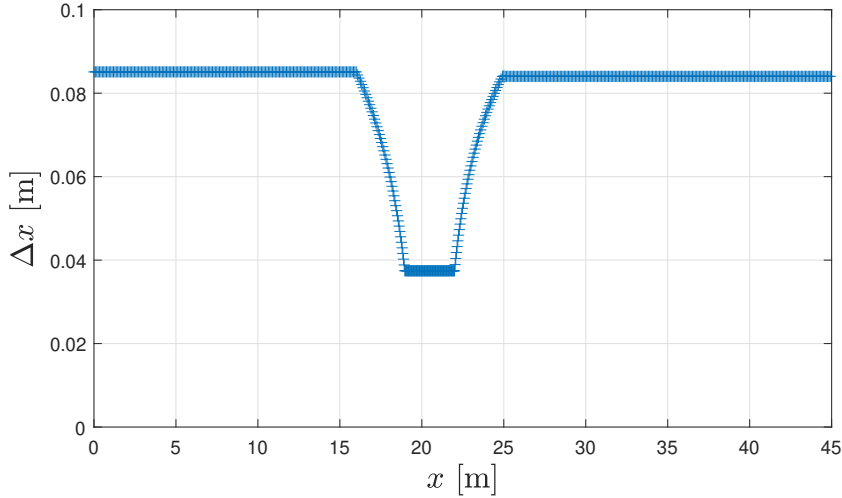
Figure 13: Horizontal distance between BEM nodes in the free surface discretization, at the start of the simulations, as a function of the x-location of the nodes.

Acknowledgment

A. Details of the NWT discretization and numerical accuracy

In the NWT simulations, 774 nodes were distributed along the boundary of the computational domain. The free surface was discretized using 601 nodes, the far end of the NWT using 31 nodes, the bottom using 101 nodes, and the wavemaker paddle using 41 nodes. In the area corresponding to the breaking location, ranging from $x = 19$ to 22 m, the distance between nodes Δx was reduced; this increased resolution yields more accurate results, in particular for the magnitude of the Γ parameter. A gradual refinement of the spatial resolution was done over 3 m zones located on either side of the area with the highest node density. Figure 13 shows the location of the BEM nodes on the free surface, at the start of the simulations ($t = 0$). A convergence study of the Γ value calculated as a function of the number of nodes on the free surface is shown in Fig. 14 for wave A7 (see Table 2). Results show that, for the simulations carried out with more than 601 nodes on the free surface (corresponding to the vertical dashed line), no significant difference is observed for the value of Γ. The orange circle corresponds to the value of Γ obtained for the base discretization, but when the flume slope is not taken into account (i.e. when the depth is equal to 2 m all along the flume). A difference of less than 4 % is observed.

The error on the volume and energy of the computational domain can be used to assess the accuracy of the BEM computations in the NWT simulations. As an example, these errors were computed for the case of wave A7. The maximum relative error on the NWT volume was 0.002%, and the maximum relative error on the energy was less than 1%, at the end of the simulation. Note, the error on the energy is computed as $(E_f - W_p)/W_p$, where E_f is the total energy of the fluid and W_p is the work of the paddle. The total energy of the fluid corresponds to the sum of its kinetic and potential energy, with the latter set to zero at the start of the simulations. The work of the paddle W_p corresponds to the work of the pressure force acting on the paddles. The time evolutions of E_f and W_p are shown in Fig. 15.

B. Detailed comparison of the experimental and numerical free-surface profiles

Most of the waves listed in Table 2 were generated and measured in Ifremer's wave flume, using a video camera, following the methodology presented in Section 2.2. Note, however, that for the measured waves, the focusing time
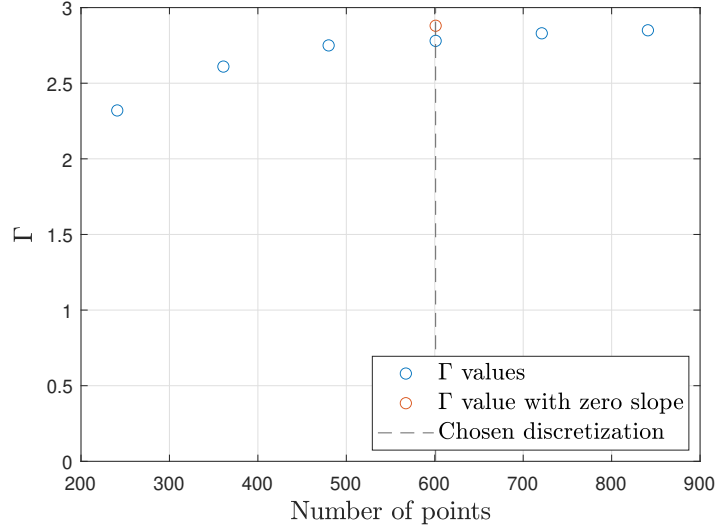
Figure 14: Evolution of the value of Γ with the number of points on the free surface. The vertical dashed line corresponds to the base discretization of 601 points on the free surface. The red circle corresponds to the value of Γ obtained with the base discretization, but without considering the longitudinal slope of the flume.
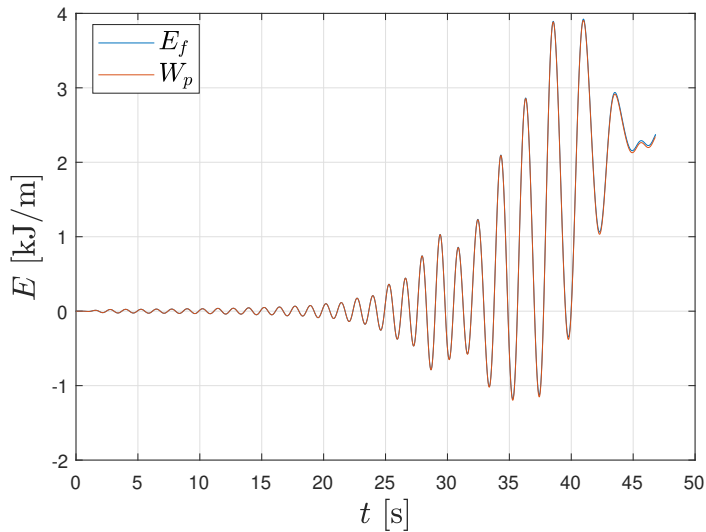

Figure 15: Comparison of the total energy of the fluid E_f and of the work of the paddle W_p computed as a function of time in the NWT, for the focused wave case A7.

was set to 30 s instead of 50 s. For this reason, the corresponding waves are denoted by a star (wave A3* corresponds to wave A3, except that $t_f = 30$ s). The non-breaking waves, as well as waves A8*, A9* and B4*, were not measured. For each of the measured waves, the time-shift Δt and difference in amplitude $\Delta \eta$ between the numerical and experimental profiles were computed 0.1 s before breaking occurred. These differences are listed in Table 4. The computation of Δt and $\Delta \eta$ is illustrated in Fig. 16, which shows the measured and numerical free-surface profiles for wave B5* 0.1 s before breaking. A time-shifted experimental profile is also shown. The employed time shift Δt was calculated such

Number	Δt [ms]	$\Delta \eta$ [m]
A3*	11.0	0.024
A4*	18.5	0.015
A5*	21.5	0.013
A6*	20.0	0.012
A7*	19.5	0.016
B2*	20.0	0.022
B3*	19.0	0.021
B5*	18.0	0.017
B6*	18.5	0.014
B7*	20.0	0.011
B8*	14.5	0.007

Table 4

Time shift and difference in amplitude between the numerical (FNPF simulations) and experimental waves, for the cases listed in Table 2, computed 0.1 s before breaking occurred: (i) Δt is the time shift between the two free-surface profiles computed with Eq. 27, and (ii) $\Delta \eta$ is the amplitude difference between the maxima of the FNPF and the measured (time shifted) profiles. Note, measured waves do not exactly correspond to those listed in Table 2, because the focusing time t_f was 30 s in experiments instead of 50 s in the model simulations. For this reason, the experimental waves are denoted by a star.
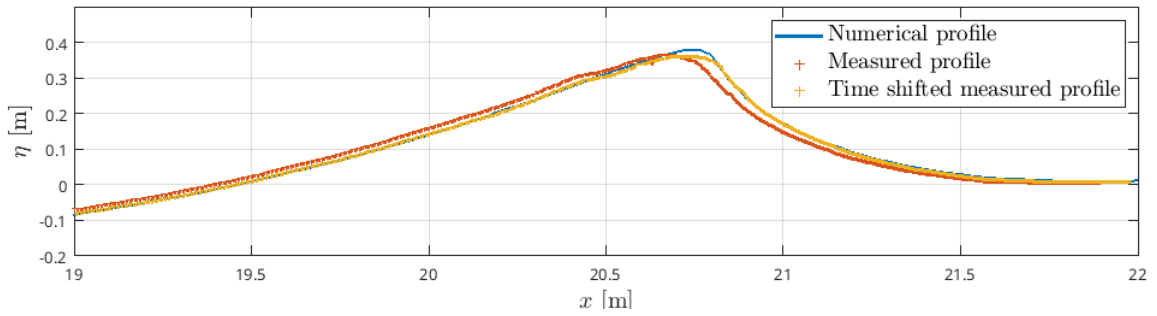

Figure 16: Comparison of the numerical and experimental free-surface profiles of wave B5*, at 0.1 s before breaking occurs. For comparison, the free-surface profile measured 18 ms later is also depicted.

that the difference between the numerical and measured profiles was minimum in the least square sense, as:

$$\Delta t = \min_{\delta t} \left(\sum_i \left(\eta_{\mathrm{FNPF}}(x_i, t_{0.1}) - \eta_{meas}(x_i, t_{0.1} + \delta t) \right)^2 \right), \tag{27}$$

where η_{FNPF} and η_{meas} denote the numerical and measured free-surface profile respectively, and x_i are the x-coordinates of the measured free-surface points. The values $\eta_{\mathrm{FNPF}}(x_i, t)$ corresponding to the experimental locations x_i are obtained by interpolating the numerical results between BEM nodes. Figure 16 shows that, except at the wave crest, the time-shifted profile is very close to the numerical profile. The crest is the wave region where the largest fluid velocities occur. As such, it is likely to be the location at which the influence of the wall on the wave shape is the largest, as a result of sidewall friction. The discrepancy in wave amplitude $\Delta \eta$ reported in Table 4 corresponds to the vertical distance between the maxima of the numerical and experimental profiles. For all the measured wave cases, the time shift Δt is less than 21.5 ms and the amplitude discrepancy $\Delta \eta$ is less than 2.5 cm.

References

Andersen, T. L. and Frigaard, P. (2014). Technical Background Material for the Wave Generation Software AwaSys 5. DCE Technical reports No. 64, Department of Civil Engineering, Aalborg University.

Ardag, D. and Resio, D. T. (2020). A new approach for modeling dissipation due to breaking in wind wave spectra. Journal of Physical Oceanography 50: 439–454, doi:10.1175/JPO-D-19-0160.1.

Banner, M. L. and Peregrine, D. H. (1993). Wave Breaking in Deep Water. Annual Review of Fluid Mechanics 25: 373–397, doi:10.1146/annurev.fl.25.010193.002105, publisher: Annual Reviews.

Barthelemy, X., Banner, M. L., Peirson, W. L., Fedele, F., Allis, M. and Dias, F. (2018). On a unified breaking onset threshold for gravity waves in deep and intermediate depth water. Journal of Fluid Mechanics 841: 463–488, doi:10.1017/jfm.2018.93.

Batlle Martin, M., Harris, J. C., Filipot, J.-F., Hulin, F., Tassin, A. and Renaud, P. (2023). Deep water focused breaking wave loads on a fixed cylinder. Coastal Engineering 186: 104397, doi:10.1016/j.coastaleng.2023.104397.

Clamond, D. and Dutykh, D. (2018). Accurate fast computation of steady two-dimensional surface gravity waves in arbitrary depth. Journal of Fluid Mechanics 844: 491–518.

Cokelet, E. D. (1977). Steep gravity waves in water of arbitrary uniform depth. Philosophical Transactions of the Royal Society of London 286: 183–230, doi:10.1098/rsta.1977.0113.

Deike, L. (2022). Mass Transfer at the Ocean–Atmosphere Interface: The Role of Wave Breaking, Droplets, and Bubbles. Annual Review of Fluid Mechanics 54: 191–224, doi:10.1146/annurev-fluid-030121-014132, publisher: Annual Reviews.

Deike, L. and Melville, W. K. (2018). Gas transfer by breaking waves. Geophysical Research Letters 45: 10–482, doi:10.1029/2018GL078758.

Derakhti, M., Banner, M. L. and Kirby, J. T. (2018). Predicting the breaking strength of gravity water waves in deep and intermediate depth. Journal of Fluid Mechanics 848: R2, doi:10.1017/jfm.2018.352.

Derakhti, M., Kirby, J. T., Banner, M. L., Grilli, S. T. and Thomson, J. (2020). A unified breaking onset criterion for surface gravity water waves in arbitrary depth. Journal of Geophysical Research: Oceans 125: e2019JC015886, doi:10.1029/2019JC015886.

Duncan, J. (1981). An experimental investigation of breaking waves produced by a towed hydrofoil. Proceedings of the Royal Society of London. A. Mathematical and Physical Sciences 377: 331–348, doi:10.1098/rspa.1981.0127.

Filipot, J.-F., Ardhuin, F. and Babanin, A. V. (2010). A unified deep-to-shallow water wave-breaking probability parameterization. Journal of Geophysical Research: Oceans 115, doi:10.1029/2009JC005448.

Ghadirian, A. and Bredmose, H. (2019). Pressure impulse theory for a slamming wave on a vertical circular cylinder. Journal of Fluid Mechanics 867: R1, doi:10.1017/jfm.2019.151.

Grilli, S., Subramanya, R., Svendsen, I. and Veeramony, J. (1994). Shoaling of solitary waves on plane beaches. Journal of Waterway, Port, Coastal, and Ocean Engineering 120: 609–628, doi:10.1061/(ASCE)0733-950X(1994)120:6(609).

Grilli, S. T. and Horrillo, J. (1997). Numerical generation and absorption of fully nonlinear periodic waves. Journal of engineering mechanics 123: 1060–1069, doi:10.1061/(ASCE)0733-9399(1997)123:10(1060).

Grilli, S. T., Skourup, J. and Svendsen, I. (1989). An efficient boundary element method for nonlinear water waves. Engineering Analysis with Boundary Elements 6: 97–107, doi:10.1016/0955-7997(89)90005-2.

Grilli, S. T. and Subramanya, R. (1996). Numerical modeling of wave breaking induced by fixed or moving boundaries. Computational Mechanics 17: 374–391, doi:10.1007/BF00363981.

Grilli, S. T., Svendsen, I. A. and Subramanya, R. (1997). Breaking criterion and characteristics for solitary waves on slopes. Journal of waterway, port, coastal, and ocean engineering 123: 102–112, doi:10.1061/(ASCE)0733-950X(1997)123:3(102).

Guyenne, P. and Grilli, S. (2006). Numerical study of three-dimensional overturning waves in shallow water. Journal of Fluid Mechanics 547: 361–388, doi:10.1017/S0022112005007317.

Hansen, H. F. and Kofoed-Hansen, H. (2017). An engineering-model for extreme wave-induced loads on monopile foundations. In ASME 2017 36th International Conference on Ocean, Offshore and Arctic Engineering. American Society of Mechanical Engineers Digital Collection.

Hulin, F. (2024). Experimental study of the hydrodynamic loads generated by breaking wave impacts on floating offshore wind turbines. PhD Thesis, ENSTA Bretagne.

Longuet-Higgins, M. (1957). The Statistical Analysis of a Random, Moving Surface. Philosophical Transactions of the Royal Society of London. Series A 249: 321–387, doi:10.1098/rsta.1957.0002.

Ma, Y., Tai, B. and Dong, G. (2024). An Extended Model for Wave Impacting on a Vertical Cylinder .

McAllister, M. L., Draycott, S., Adcock, T. a. A., Taylor, P. H. and Bremer, T. S. v. d. (2019). Laboratory recreation of the Draupner wave and the role of breaking in crossing seas. Journal of Fluid Mechanics 860: 767–786, doi:10.1017/jfm.2018.886.

Mohanlal, S., Harris, J. C., Yates, M. L. and Grilli, S. T. (2023). Unified depth-limited wave breaking detection and dissipation in fully nonlinear potential flow models. Coastal Engineering 183: 104316, doi:10.1016/j.coastaleng.2023.104316.

Ohana, J. and Bourdier, S. (2014). Tank test related instrumentation and best practice, Ref. Deliverable 4.01EC, https://archimer.ifremer.fr/doc/00214/32572/. Tech. rep.

Paulsen, B. T., Bredmose, H. and Bingham, H. B. (2014). An efficient domain decomposition strategy for wave loads on surface piercing circular cylinders. Coastal Engineering 86: 57–76, doi:10.1016/j.coastaleng.2014.01.006.

Paulsen, B. T., Sonneville, B. d., Meulen, M. v. d. and Jacobsen, N. G. (2019). Probability of wave slamming and the magnitude of slamming loads on offshore wind turbine foundations. Coastal Engineering 143: 76–95, doi:https://doi.org/10.1016/j.coastaleng.2018.10.002.

Perlin, M., Choi, W. and Tian, Z. (2013). Breaking Waves in Deep and Intermediate Waters. Annual Review of Fluid Mechanics 45: 115–145, doi:10.1146/annurev-fluid-011212-140721, publisher: Annual Reviews.

Phillips, O. M. (1966). The dynamics of the upper ocean.

Rapp, R. J. and Melville, W. K. (1990). Laboratory measurements of deep-water breaking waves. Philosophical Transactions of the Royal Society of London. Series A, Mathematical and Physical Sciences 331: 735–800, doi:10.1098/rsta.1990.0098, publisher: Royal Society.

Saket, A., Peirson, W. L., Banner, M. L., Barthelemy, X. and Allis, M. J. (2017). On the threshold for wave breaking of two-dimensional deep water wave groups in the absence and presence of wind. Journal of Fluid Mechanics 811: 642–658, doi:10.1017/jfm.2016.776.

Stringari, C. E., Prevosto, M., Filipot, J.-F., Leckler, F. and Guimarães, P. V. (2021). A New Probabilistic Wave Breaking Model for Dominant Wind-Sea Waves Based on the Gaussian Field Theory. Journal of Geophysical Research: Oceans 126: e2020JC016943, doi:10.1029/2020JC016943.

Varing, A., Filipot, J.-F., Grilli, S., Duarte, R., Roeber, V. and Yates, M. (2021). A new definition of the kinematic breaking onset criterion validated with solitary and quasi-regular waves in shallow water. Coastal Engineering 164: 103755, doi:10.1016/j.coastaleng.2020.103755.

Wienke, J. and Oumeraci, H. (2005). Breaking wave impact force on a vertical and inclined slender pile - theoretical and large-scale model investigations. Coastal Engineering 52: 435–462, doi:10.1016/j.coastaleng.2004.12.008.